Chapter 2
Theory

2.1 Relativistic Hydrodynamics

Since jets are collimated flows of relativistic particles, it is necessary to introduce the basic concepts of relativistic hydrodynamics. We will study the jet evolution far from the formation region. Thus, we use the equations of special-relativistic hydrodynamics. The two basic equations in special relativistic hydrodynamics are the conservation of mass and the energy-momentum. These two conservation laws can be written in the following form:

$$\partial_\mu \left(\rho u^\mu\right) = 0 \tag{2.1}$$
$$\partial_\mu \left(T^{\mu\nu}\right) = 0, \tag{2.2}$$

where $\mu, \nu = 0, 1, 2, 3$, ρ is the density, u the four velocity and $T^{\mu\nu}$ is energy-momentum tensor:

$$T^{\mu\nu} = \rho h u^\mu u^\nu + p g^{\mu\nu}, \tag{2.3}$$

with p the pressure, $g^{\mu\nu}$ the metric tensor (here Minkowski space-time) and $h = c^2 + \epsilon + p/\rho$ the specific enthalpy, where ϵ is the specific internal energy. The four-velocity can be written as $u^\mu = \Gamma(t, v^1, v^2, v^3)$ by introducing the Lorentz factor $\Gamma = 1/\sqrt{1 - u^i u_i / c^2}$. The set of equations is closed by the equation of state, i.e., the relation between pressure and density. Throughout this work we use an ideal equation of state:

$$p = \left(\hat{\gamma} - 1\right) \rho \epsilon, \tag{2.4}$$

where $\hat{\gamma}$ is the adiabatic index. Some additional parameters which can be helpful in describing the fluid properties are the sound speed, c_s, and the Mach number, $M = u/c_s$. Notice that we use a Newtonian definition of the Mach number throughout

This chapter is partially published in Fromm et al. (2011, 2013a, b).

C. Fromm, *Spectral Evolution in Blazars*, Springer Theses,
DOI 10.1007/978-3-319-10768-4_2

this work. The relativistic sound speed is given by:

$$c_s = \sqrt{\frac{\hat{\gamma}\, p}{\rho h}} \tag{2.5}$$

To solve these equations numerically it is necessary to rewrite them in terms of conserved fluxes and recover the physical variables (p, ρ, and v) from conserved ones. For a more detailed derivation of the RHD equations see, e.g., Martí and Müller (1999); Martí et al. (1997).

The conservation equations (2.1) and (2.2) imply that the flux through a the cross-section of the jet is conserved. Thus, for a time independent flow these equations can be written for two arbitrary locations as:

$$\Gamma_0 \rho_0 v_0 R_0^2 = \Gamma_1 \rho_1 v_1 R_1^2 \tag{2.6}$$

$$\Gamma_0^2 h_0 v_0 R_0^2 = \Gamma_1^2 h_1 v_1 R_1^2, \tag{2.7}$$

where we assume a one-dimensional flow and the subscripts 0 and 1 correspond to two different locations along the jet. In the following, we present the application of the RHD equations to extragalactic jets, where we focus on two possible configurations: (a) pressure-matched (conical) jets and (b) over-pressured (non-conical) jets.

Throughout this work we do not include the magnetic field in the equations, i.e., we take a pure RHD approach, and, when needed, compute the magnetic field from the pressure, p, and assuming that the magnetic energy density is a fraction, ϵ_b of thermal energy density ($\epsilon_b = 1$ corresponds to equipartition between magnetic and thermal energy density):

$$B = \sqrt{\frac{8\pi p \epsilon_b}{\hat{\gamma} - 1}} \tag{2.8}$$

2.1.1 Pressure-Matched Jets

The shape of the jet will be conical if there is a transversal pressure match with the ambient medium and if there is a gradient in the ambient pressure. The opening angle, φ, of such a freely expanding jet can be calculated from the Mach number, M_0, and the bulk Lorentz factor, Γ_0, at the jet nozzle (Begelman et al. 1984):

$$\varphi = \arctan\left(\frac{1}{\Gamma_0 M_0}\right) \tag{2.9}$$

In Fig. 2.1 we present the 2D distribution of the logarithm of rest mass density for a conical jet from a RHD simulation (axis are not drawn to scale). The strips at the

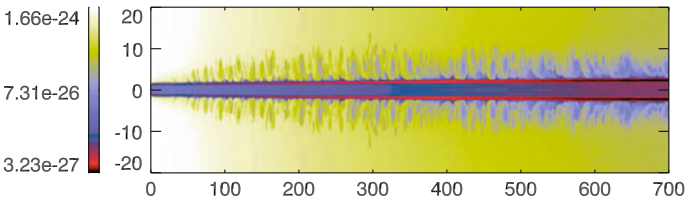

Fig. 2.1 2D distribution of the logarithm of the rest mass density from a RHD simulation of a conical jet

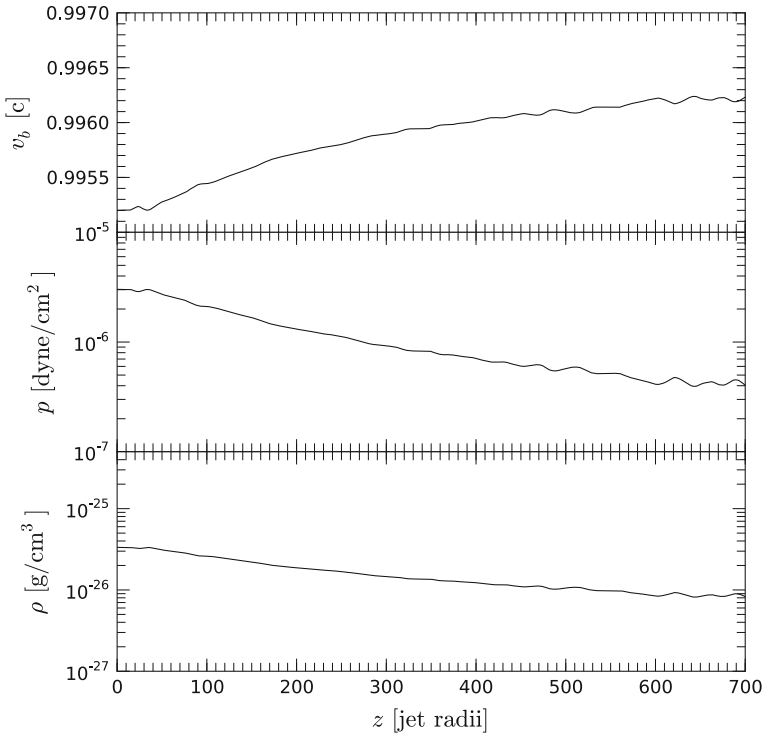

Fig. 2.2 Variation of the intrinsic parameters along the jet axis for a conical jet. *Top* evolution of velocity in terms of speed of light; *Middle* evolution of pressure; *Bottom* evolution of density

boundary between jet and ambient medium are Kelvin-Helmholtz (K-H) instabilities, which are generated due to the velocity difference between the two fluids.

In a hot conical jet with constant opening angle, φ, the fluid speed, v, increases with distance from the jet nozzle and the density, ρ, and pressure, p, decrease with distance. This behavior can be seen in Fig. 2.2 which shows the variation of the intrinsic parameters along the jet axis. The evolution of these parameters can be directly calculated from Eqs. 2.6 and 2.7 if the conditions at the jet nozzle and $\hat{\gamma}$ are known (see, e.g., Hardee and Eilek 2011).

2.1.2 Over-Pressured Jets

In contrast to a conical jet, there is no transversal pressure equilibrium in over-pressured jets. Therefore, the shape of the jet will not be conical and the evolution of the intrinsic parameters is not monotonously de- or increasing. Owing to the supersonic nature of the flow, recollimation or standing shocks will form along the jet. The formation of a standing shock can be described in the following way: The unbalance between the jet pressure and the pressure of the ambient medium at the jet nozzle leads to an opening of the jet. Due to the conservation laws of hydrodynamics, this opening results in a decrease of the density, the pressure and the magnetic field intensity in the jet. The finite speed of the sound waves in the jet is responsible for an over-expansion followed by a recollimation of the jet that gives rise to the formation of a shock. During this collimation process the jet radius decreases and the shock leads to an increase of the pressure, density, and magnetic field intensity. Again, the finite speed of the sound waves is responsible for a over-collimation of the jet. This interplay between over-expansion and over-collimation leads to the picture of a pinching flow, i.e., a continuous change of the width along the jet axis, in contrast to conical jets. The intrinsic physical parameters (pressure, density, and magnetic field) along a pinching jet show a sequence of local maxima and minima (see, e.g.,Daly and Marscher 1988; Falle 1991; Komissarov and Falle 1997; Perucho and Martí 2007; Nalewajko and Sikora 2009).

The Eqs. 2.6 and 2.7 cannot be directly used to derive the evolution of the intrinsic parameters. However, some properties of the recollimation shocks can be derived from analytical models. Daly and Marscher (1988) derived the position of the recollimation shock, $L_{\max}$, and the maximum jet width, $R_{\max}$ assuming a homogeneous ambient medium and ultra-relativistic equation of state, i.e., $\hat{\gamma} = 4/3$ (relativistic $e^- e^+$ plasma).

$$L_{\max} \sim 3.3 \Gamma_0 R_0 d_k \tag{2.10}$$

$$R_{\max} \sim \left(1 + 1.9 \left[\frac{1 - d_k^{-1/4}}{2 d_k^{-1/4} - 1}\right]\right) R_0, \tag{2.11}$$

where Γ_0 and R_0 are the bulk Lorentz factor and the jet radius at the jet nozzle and $d_k = p_0 / p_{\text{ext}}$ is the pressure ratio between the pressure in the jet and in the ambient medium at the same position. In the case of a homogeneous ambient medium the distance between the recollimation shocks is constant and the jump in the intrinsic values are equal. In this simplified model, each recollimation shock could be regarded as a new jet nozzle.

In a similar way to Daly and Marscher (1988), Komissarov and Falle (1997) derived the properties of a recollimation shock in an ambient medium with decreasing pressure $p_{\text{ext}} = a L^{-\eta}$, using an approximation for the pressure behind the recollimation shock that allows to solve the shock-jump conditions analytically. They derived the following relations for $L_{\max}$, $R_{\max}$, and, $L(R_{\max})$, the location of the maximum jet width and reconfinment angle φ_{conf}

$$L_{\max} = \left[\frac{\varphi\left(1-\frac{\eta}{2}\right)}{A}\right]^{1/\left(1-\frac{\eta}{2}\right)} \left[1+\frac{1}{\left(1-\frac{\eta}{2}\right)}\chi^{1-\frac{\eta}{2}}\right]^{1/\left(1-\frac{\eta}{2}\right)} \tag{2.12}$$

$$L\left(R_{\max}\right) = \left(\frac{\varphi}{A}\right)^{1/\left(1-\frac{\eta}{2}\right)} \left(\frac{1-\frac{\eta}{2}}{2-\frac{\eta}{2}}\right)^{1/\left(1-\frac{\eta}{2}\right)} \left[1+\frac{1}{1-\frac{\eta}{2}}\chi^{1-\frac{\eta}{2}}\right]^{1/\left(1-\frac{\eta}{2}\right)} \tag{2.13}$$

$$R_{\max} = \left[\frac{1-\frac{\eta}{2}}{2+\frac{\eta}{2}}\right]^{\frac{4+\eta}{2+\eta}} \frac{R_0}{\chi} \tag{2.14}$$

$$\varphi_{\text{conf}} = \left(1-\frac{\eta}{2}\right)\varphi\left[1+\frac{1}{1+\frac{\eta}{2}}\chi^{1-\frac{\eta}{2}}\right] \tag{2.15}$$

where $A = (a/K)^{1/2}$, with K defined as

$$K = \frac{\mu L u_j}{\pi \varphi^2 \Gamma_j}, \tag{2.16}$$

L being the total kinetic power of the jet. The parameter χ describes the influence of the initial jet radius at the jet nozzle, R_0, and is defined as:

$$\chi = \frac{R_0 A^{1/\left(1-\frac{\eta}{2}\right)}}{\varphi^{(4+\eta)/(2-\eta)}} \tag{2.17}$$

Figure 2.3 shows the influence of a gradient in the ambient medium on the shape of the jet and the formation of recollimation shocks. The top panel in Fig. 2.3 shows the distribution of the rest mass density in an ambient medium with decreasing pressure and the bottom panel in a homogeneous ambient medium. The plots show that in the case of a decreasing pressure in the ambient medium the number of recollimation shocks is smaller and their separation is increasing with distance. In addition, the length of the recollimation zone is increasing with distance if there is a gradient in the ambient medium.

The difference between both cases becomes more visible in the evolution of ρ, p, and v along the jet axis (see Fig. 2.4) The different panels in Fig. 2.4 show the evolution of the velocity (top), the pressure (middle) and rest-mass density (bottom), where the black solid line corresponds to the model with decreasing pressure and the blue solid line to the one with homogeneous ambient medium. As mentioned before, in the case of a homogeneous ambient medium, the axial values at the location of the recollimation shock are comparable to the values at the jet nozzle. On the other hand, for the decreasing ambient medium, the increase of the intrinsic values at the position of the recollimation shock is decreasing with distance.

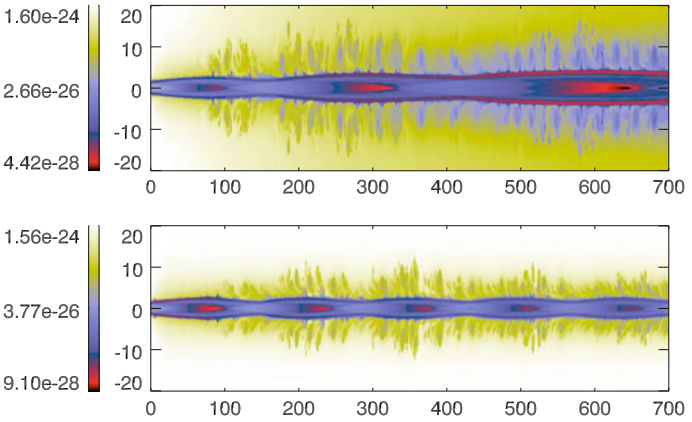

Fig. 2.3 2D distribution of the logarithm of the rest mass density from a RHD simulation of an over-pressured jet. *Top* over-pressured jet in decreasing ambient medium; *Bottom* over-pressured jet in constant ambient medium

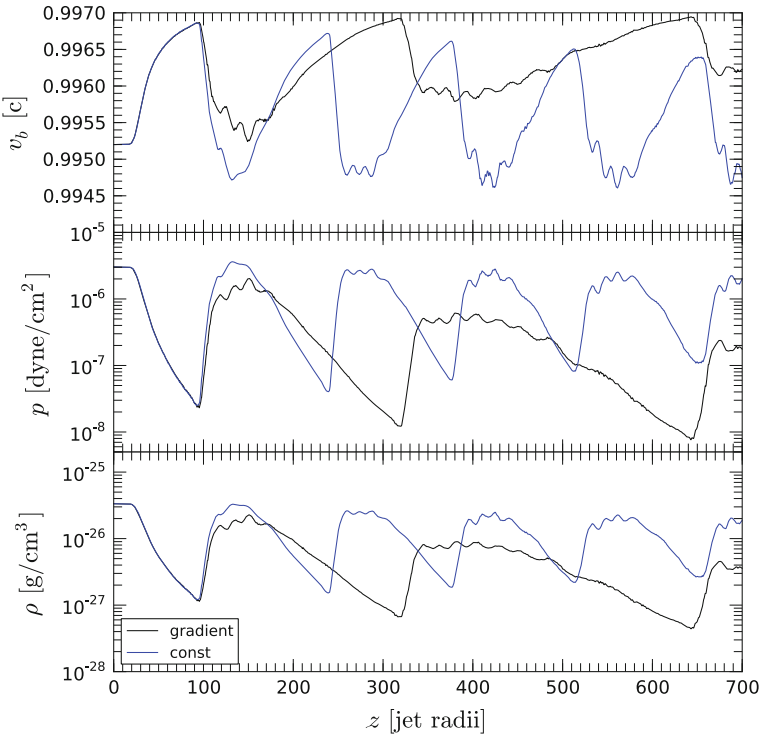

Fig. 2.4 Variation of the intrinsic parameters along the jet axis for an over-pressured jet. The *black lines* correspond to a model with decreasing ambient medium and the *red lines* to a model with constant ambient medium. *Top* evolution of velocity in terms of speed of light; *Middle* evolution of pressure; *Bottom* evolution of rest-mass density

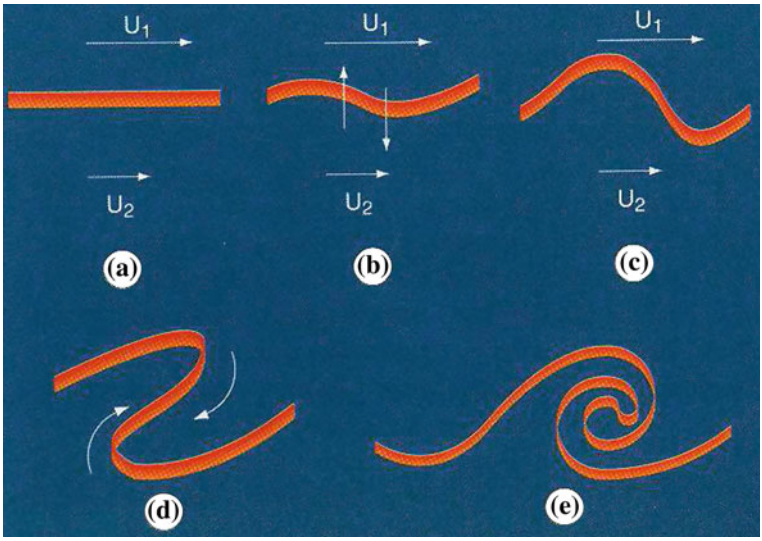

Fig. 2.5 Illustration of the growth of K-H instabilities taken from Perucho (2005)

2.1.3 Kelvin-Helmholtz (K-H) Instability

Relativistic flows such as jets are affected by several kinds of fluid instabilities (see, e.g., Hardee et al. 1996; Perucho 2012) The most relevant instability in case of relativistic jets are K-H instability, which grow between two flows with non-vanishing relative velocity at the transition layer between the jet and the ambient medium. Figure 2.5 shows an illustration of the generation of K-H instability.

The development of K-H instability can be explained by the Bernoulli effect. The relative difference in the velocities at the contact surface leads to a drop in the transversal pressure forcing the fluid to increase its transversal velocity. Thus the fluid propagates into other medium, from the jet into ambient medium and vice versa (indicated by b and c in Fig. 2.5). The continuation of this effect leads to a displacement of the fluid and to the mass loading of the jet with material from the ambient medium (see d and e in Fig. 2.5). The mathematical treatment of the instability problem uses the classical perturbation theory, i.e., adding a perturbation term to the initial parameters (e.g. $p = p_0 + p_1$) (see, e.g., Hardee 2000). In general the pressure perturbation, p_1, in cylindrical geometry can be written in the form of $p_1 = \exp(i(kz \pm n\phi - \omega t))$ where k is the longitudinal wavenumber, n the azimuthal wave number, and ω the frequency. The different modes of K-H instabilities can thus be classified by their value of n and k. For example $n = 0$ corresponds to a pinching mode and $n = 1$ to a helical mode. Each mode, n, has a surface and multiple body modes (Perucho 2005).

2.2 Synchrotron Radiation

Here, we review the basic equations of synchrotron self absorption and present the relations needed for the performed spectral analysis (see e.g., Pacholczyk 1970; Marscher 1987; Lobanov 1998; Türler et al. 1999).

The emission, ϵ_ν, and absorption coefficients, κ_ν, of a power law distribution of relativistic electrons, $N(E) = K E^{-s}$, in the presence of a magnetic field, B, where K is the normalization coefficient of the distribution and s the spectral slope, can be written as (see Pacholczyk 1970, for details):

$$\epsilon_\nu = c_\epsilon(s) K (B \sin\varphi)^{(s+1)/2} \nu^{-(s-1)/2} \tag{2.18}$$

$$\kappa_\nu = c_\kappa(s) K (B \sin\varphi)^{(s+2)/2} \nu^{-(s+4)/2}, \tag{2.19}$$

where φ is the pitch angle and ν is the frequency. The constants $c_\epsilon(s)$ and $c_\kappa(s)$ are given by:

$$c_\epsilon(s) = \frac{\sqrt{3} e^3}{16\pi m_e c^2} \left(\frac{3e}{2\pi m_e^3 c^5}\right)^{\frac{s-1}{2}} \left(\frac{s+\frac{7}{3}}{s+1}\right) \hat{\Gamma}\left(\frac{3s-1}{12}\right) \hat{\Gamma}\left(\frac{3s+7}{12}\right) \tag{2.20}$$

$$c_\kappa(s) = \frac{\sqrt{3}\pi}{72} e m_e^5 c^{10} \left(\frac{3e}{2\pi m_e^3 c^5}\right)^{\frac{s+4}{2}} \left(\frac{s+10}{3}\right) \hat{\Gamma}\left(\frac{3s+2}{12}\right) \hat{\Gamma}\left(\frac{3s+10}{12}\right), \tag{2.21}$$

with e the electron charge, m_e the electron rest-mass, c the speed of light (all in cgs units) and $\hat{\Gamma}$ the complete Euler Gamma-function. For a random magnetic field, the constants above have to be averaged over the pitch angle, i.e., multiplied by $c_{\epsilon,b}$ and $c_{\kappa,b}$, respectively:

$$c_{\epsilon,b}(s) = \frac{\sqrt{\pi}}{2} \hat{\Gamma}\left(\frac{s+5}{4}\right) \left(\hat{\Gamma}\left(\frac{s+7}{4}\right)\right)^{-1} \tag{2.22}$$

$$c_{\kappa,b}(s) = \frac{\sqrt{\pi}}{2} \hat{\Gamma}\left(\frac{s+6}{4}\right) \left(\hat{\Gamma}\left(\frac{s+8}{4}\right)\right)^{-1}. \tag{2.23}$$

The specific intensity, I_ν, can be written as:

$$I_\nu = \frac{\epsilon_\nu}{\kappa_\nu} \left(1 - e^{-\tau_\nu}\right), \tag{2.24}$$

where ϵ_ν and κ_ν are the emission and absorption coefficients and $\tau_\nu = \kappa_\nu x$ is the optical depth, with x the distance along the line of sight. Defining ν_1 as the frequency at which $\tau_\nu = 1$, Eq. 2.24 takes the following form (Pacholczyk 1970):

$$I_\nu = I_{\nu_1} \left(\frac{\nu}{\nu_1}\right)^{\alpha_t} \left[1 - \exp\left(\frac{\nu}{\nu_1}\right)^{\alpha_0 - \alpha_t}\right], \tag{2.25}$$

where α_t is the optically thick spectral index ($\alpha_t = 5/2$ for a homogenous source) and $\alpha_0 < 0$ is the optically thin spectral index. The optically thin spectral index is connected to the spectral slope, s, by the following relation:

$$\alpha_0 = -\frac{(s-1)}{2}. \tag{2.26}$$

Using the transformation from intensities to flux densities, Eq. 2.25 can be expressed in terms of the observed turnover flux density, S_m, and turnover frequency, ν_m (Türler et al. 1999).

$$S_\nu \approx S_m \left(\frac{\nu}{\nu_m}\right)^{\alpha_t} \frac{1 - \exp\left(-\tau_m \left(\nu/\nu_m\right)^{\alpha_0 - \alpha_t}\right)}{1 - \exp\left(-\tau_m\right)}, \tag{2.27}$$

where $\tau_m \approx 3/2 \left(\sqrt{1 - \frac{8\alpha_0}{3\alpha_t}} - 1\right)$ is the optical depth at the turnover. Depending on the value of ν/ν_m, Eq. 2.27 describes an optically thick ($\nu < \nu_m$) or optically thin ($\nu > \nu_m$) spectrum with their characteristic shapes $S_\nu \propto \nu^{5/2}$ and $S_\nu \propto \nu^{-(s-1)/2}$, respectively. In Fig. 2.6 we present an example of a synchrotron spectrum computed from Eq. 2.27.

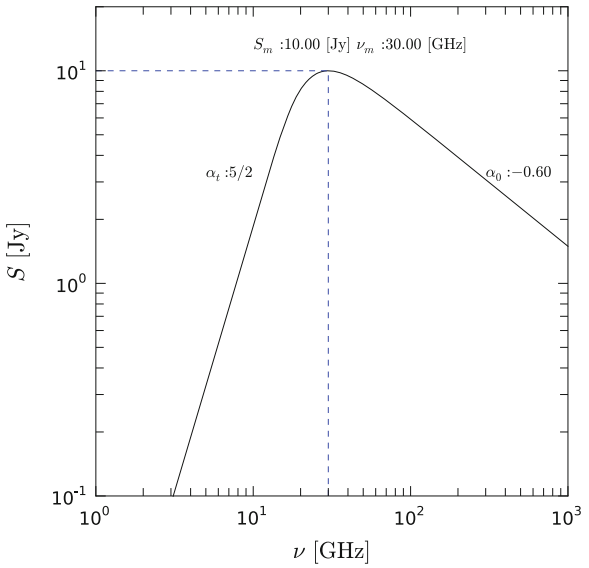

Fig. 2.6 Synchrotron spectrum with a turnover position at $\nu_m = 30\,\text{GHz}$ and $S_m = 10\,\text{Jy}$ and an optically thin spectral index of $\alpha_0 = -0.6$

2.2.1 Magnetic Field, B, and Particle Density, K

Once the turnover frequency, ν_m, and the turnover flux density, S_m, are obtained, we can derive estimates for the magnetic field, B, and the normalization coefficient, K, (see e.g., Marscher 1987). Following Lind and Blandford (1985), the emission, ϵ_ν, and absorption, κ_ν, coefficient have to be corrected for relativistic and cosmological effects. In the following, primed variables correspond to the observers frame and the equations are derived for a random magnetic field (isotropic pitch angle, φ) with all parameters in cgs units:

$$\epsilon'_{\nu'} = \delta^2 \epsilon_{(\nu'(1+z)/\delta)} \tag{2.28}$$

$$\kappa'_{\nu'} = \delta^{-1} \kappa_{(\nu'(1+z)/\delta)} \tag{2.29}$$

with $\delta = \Gamma^{-1}\,(1 - \beta\cos\vartheta)^{-1}$ the Doppler factor and z the redshift. The optically thin flux, $S_{\nu',\,\mathrm{thin}} = \Omega\epsilon'_\nu R$, is given by:

$$S_{\nu',\,\mathrm{thin}} = \frac{\pi}{D_l^2} c_\epsilon(s) c_{\epsilon,b}(s) (1+z)^{-\frac{s-3}{2}} R^3 \delta^{\frac{s+5}{2}} K B^{\frac{s+1}{2}} \nu'^{-\frac{s-1}{2}}, \tag{2.30}$$

and the optical depth, τ_ν, is:

$$\tau'_{\nu'} = c_\kappa(s) c_{\kappa,b}(s) (1+z)^{-\frac{s-4}{2}} R \delta^{\frac{s+4}{2}} K B^{\frac{s+2}{2}} \nu'^{-\frac{s+4}{2}} \tag{2.31}$$

Using the obtained turnover values, the flux density, S'_ν, in Eq. 2.30 and the frequency, ν', in Eq. 2.31 can be replaced by the turnover flux density, S'_m, and the turnover frequency, ν'_m:

$$S'_m = \pi D_l^{-2} c_\epsilon(s) c_{\epsilon,b}(s) (1+z)^{-\frac{s-3}{2}} R^3 \delta^{\frac{s+5}{2}} K B^{\frac{s+1}{2}} \nu_m'^{-\frac{s-1}{2}} \tag{2.32}$$

$$\tau'_m = c_\kappa(s) c_{\kappa,b}(s) (1+z)^{-\frac{s-4}{2}} R \delta^{\frac{s+4}{2}} K B^{\frac{s+2}{2}} \nu_m'^{-\frac{s+4}{2}} \tag{2.33}$$

The equations above can be solved for the magnetic field, B, and the normalization coefficient, K:

$$B = \frac{\pi^2}{D_l^4} \left[\frac{c_\epsilon(s) c_{\epsilon,b}(s)}{c_\kappa(s) c_{\kappa,b}(s)}\right]^2 (1+z)^7 R^4 \delta \nu_m'^5 S_m'^{-2} \tau_m'^2 \tag{2.34}$$

$$K = \frac{D_l^{2s+4}}{(\pi)^{s+2}} \left[c_\epsilon(s) c_{\epsilon,b}(s)\right]^{-(s+2)} \left[c_\kappa(s) c_{\kappa,b}(s)\right]^{s+1} (1+z)^{-(3s+5)} R^{-(2s+5)} \delta^{-(s+3)} \tau_m'^{-(s+1)} S_m'^{s+2} \nu_m'^{-(2s+3)}. \tag{2.35}$$

2.2.1.1 Number of Particles, N, Relativistic Energy Density, U_e, and Magnetization σ

The number of particles, N, and the relativistic energy density, U_e, can be calculated by integrating the distribution function $N(E) = KE^{-s}$ within the limits $E_1 = \gamma_{\rm min} m_e c^2$ and $E_2 = \gamma_{\rm max} m_e c^2$, where $\gamma_{\rm min,max}$ are the lower and upper electron Lorentz factors:

$$N = \frac{K}{s-1}\left(m_e c^2\right)^{1-s} \gamma_{\rm min}^{1-s}\left[1 - \left(\frac{\gamma_{\rm max}}{\gamma_{\rm min}}\right)^{1-s}\right] \tag{2.36}$$

$$U_e = \begin{cases} \frac{K}{2-s}\left(m_e c^2\right)^{2-s} \gamma_{\rm max}^{2-s}\left[1 - \left(\frac{\gamma_{\rm min}}{\gamma_{\rm max}}\right)^{2-s}\right] & \text{if } 1 < s < 2 \\ K \ln\left(\frac{\gamma_{\rm max}}{\gamma_{\rm min}}\right) & \text{if } s = 2 \\ \frac{K}{s-2}\left(m_e c^2\right)^{2-s} \gamma_{\rm min}^{2-s}\left[1 - \left(\frac{\gamma_{\rm max}}{\gamma_{\rm min}}\right)^{2-s}\right] & \text{if } s > 2 \end{cases} \tag{2.37}$$

Together with the magnetic energy density $U_b = B^2/(8\pi)$ we can define the magnetization parameter

$$\sigma_{\rm mag} = \frac{U_b}{U_e}, \tag{2.38}$$

and can test whether the emitting region is in equipartition, $\sigma_{\rm mag} = 1$, or not.

2.2.1.2 Evolution of the Electron Lorentz Factor

Marscher (1987) pointed out that the energy limits, $E_{\rm min} = \gamma_{\rm min} m_e c^2$ and $E_{\rm max} = \gamma_{\rm min} m_e c^2$ are difficult to extract from observations and require a meaningful set of assumptions. Here we follow the suggestions of Marscher (1987) and present a first order approximation for the evolution of the lower, $\gamma_{\rm min}$, and upper, $\gamma_{\rm max}$ electron Lorentz factor. We consider two different jet geometries, (i) a conical pressure matched jet ($d_k = p_0/p_a = 1$) and (ii) an over-pressured jet ($d_k \neq 1$). We also assume that Compton losses can be neglected at parsec scale distances (Mimica et al. 2009) and we compute the evolution of the electron Lorentz factor assuming (iii) only adiabatic losses and (iv) synchrotron and adiabatic losses. In the following section we use an adiabatic index $\hat{\gamma} = 4/3$, which corresponds to a ultra-relativistic $e^- e^+$ plasma.

Since the expansion of the jet implies the adiabatic energy losses, the first step for both jet models includes the calculation of the jet profile.

Conical jet: In the case of a pressure matched jet, the profile will be of conical shape and it is characterized by its radius at the jet nozzle, R_0, and its opening angle φ. The opening angle, φ, can be obtained either from the measured bulk Lorentz factor

$\varphi \sim 1/\Gamma$ (e.g., Konigl 1981), or from the transversal size of the jet (e.g., Pushkarev et al. 2009). The jet width at the nozzle, R_0, can be calculated in the following way:

$$R_0 = R_j - r_{j-0} \tan \varphi, \tag{2.39}$$

with R_j the jet width obtained at a position r_j, where the jet can be transversally resolved and r_{j-0} is the distance to the jet nozzle including the opacity shift correction (see Sect. 2.46). Finally the jet width for a conical geometry can be written as power law:

$$R(r) = R_0 \left(\frac{r}{r_0}\right)^{\epsilon}, \tag{2.40}$$

where $\epsilon = 1$ and r_0 is a normalization distance.

Overpressured jet: The initial over-pressure at the jet nozzle leads to the formation of recollimation shocks further downstream (e.g., Daly and Marscher 1988). Such stationary features can be detected and identified using VLBI observations. For the calculation of the jet width at the nozzle we use the approximation presented by Daly and Marscher (1988):

$$R_0 \sim \frac{r_{\max}}{3.3\Gamma_0 d_k},$$

where $r_{\max}$ is the de-projected distance between the jet nozzle and the recollimation shock, Γ_0 is the bulk Lorentz factor of the fluid and $d_k = p_0/p_{\text{ext}}$ is the overpressure. Here we use values obtained at the location of the standing shock which is justified by the fact that the conditions (pressure and density) at the position of the standing shock wave are roughly the same as those at the jet nozzle (a homogeneous ambient medium). If we assume a locally constant ambient medium, the distance between the jet nozzle and the location of maximal jet width is $r(R_{\max}) \sim 0.5 \cdot r_{\max}$ (Komissarov and Falle 1997). Together with R_0, we can now derive the jet opening index, ϵ, for $r < r(R_{\max})$. For $r > (R_{\max})$ the jet will start to collimate and will reach a local minimum at the position of the standing shock. As in the case of the jet opening region we can, given the jet width at the position of the standing shock, compute ϵ for this region. If there are additional recollimation shocks with known distance from the previous shock and jet width, one can proceed as in the case of the first recollimation shock and define the jet geometry.

Adiabatic and synchrotron losses: In order to provide an estimate for the variation of the electron Lorentz factor γ along the jet, we have to solve the energy-loss equation, which includes both, radiative and adiabatic losses (see, e.g., Georganopoulos and Marscher 1998; Mimica et al. 2009)

$$\frac{d\gamma}{dr} = -\left(\frac{d\gamma}{dr}\right)_{\text{syn}} - \left(\frac{d\gamma}{dr}\right)_{\text{adi}}, \tag{2.41}$$

where γ corresponds to the electron Lorentz factor and r to the distance along the jet. The synchrotron and adiabatic losses are given by (Fromm et al. in preparation):

$$\left(\frac{d\gamma}{dr}\right)_{\rm syn} = \left(\frac{2}{3}\right)^2 \frac{e^4}{m_e^3 c^6} \gamma^2 B^2 \tag{2.42}$$

$$\left(\frac{d\gamma}{dr}\right)_{\rm adi} = \frac{\gamma}{3} \frac{d\ln\rho}{dz} \tag{2.43}$$

If we parametrize the magnetic field, $B = B_0 (R/R_0)^{-b}$, and the jet geometry, $R = R_0 (r/r_0)^{\epsilon}$, the energy loss equation can be simplified to:

$$\frac{d\gamma}{dr} = -\left(\frac{2}{3}\right)^2 \frac{e^4}{m_e^3 c^6} \gamma^2 B_0^2 \left(\frac{r}{r_0}\right)^{-2\epsilon b} - \frac{\gamma\epsilon}{r} \tag{2.44}$$

This differential equation has the following analytical solution (Fromm et al., in preparation):

$$\gamma(r) = \frac{\gamma_0 \left(\epsilon + 2\epsilon b - 1\right) r_0^{\epsilon}}{-C\gamma_0 r r_0^{\epsilon} + r^{\epsilon} \left(\frac{r}{r_0}\right)^{2\epsilon b} \left(\epsilon + 2\epsilon b + C\gamma_0 r_0 - 1\right)} \left(\frac{r}{r_0}\right)^{2\epsilon b}, \tag{2.45}$$

where $C = \left(\frac{2}{3}\right)^2 (e^4)/(m_e^3 c^6) B_0^2$ and $\gamma_0 = \gamma\,(r_0)$ corresponds to the initial value.

As an example, we use the values tabulated in Table 2.1 and calculate the evolution of the electron Lorentz factors along the jet. In Fig. 2.7, we show the evolution of the electron Lorentz factor for an over-pressured (left panels) and conical jet (right panels). The X-axis are drawn in pc (bottom) and in mas (top). The panels show (from top to bottom) the evolution of the jet width with distance along the jet, the evolution

Table 2.1 Parameters used in the calculation of $\gamma_{\rm min}$ and $\gamma_{\rm max}$ presented in Fig. 2.7

Parameter	Symbol	Value	Source
Normalization of B-field	B_0	0.1 G	VLBI[b]
Exponent B-field evolution	b	1.0	VLBI[b]
Normalization distance	r_0	1.0 pc	VLBI[b]
Viewing angle	ϑ	2.6°	VLBI[a]
Bulk Lorentz factor	Γ_0	13	VLBI[a]
Pressure matched jet	d_k	3	VLBI[c]
Jet opening index	ϵ	0.6, 0.8, −0.5, 1.2	VLBI[b]
Electron Lorentz factor	$\gamma_{\rm min,max}$	100, 1×10^5	Theory[d]

[a] Taken from Chap. 4
[b] Taken from Chap. 5
[c] Taken from Jorstad et al. (2005b)
[d] T aken from Mimica et al. (2009)

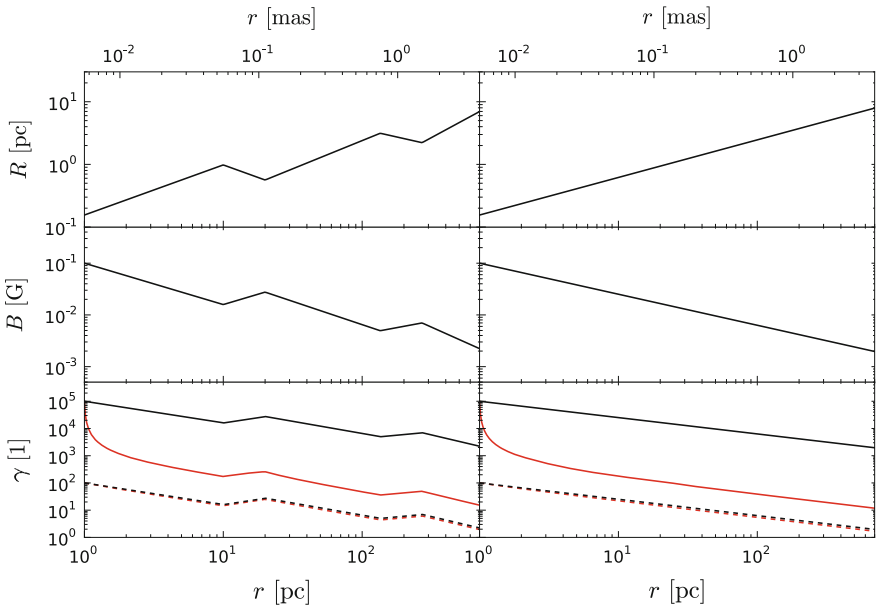

Fig. 2.7 Evolution of source intrinsic parameters for an over-pressured jet, $d_k \neq 1$, (*left panels*) and for a conical jet, $d_k = 1$, (*right panels*). The *upper panels* show the variation of the jet width, R, in pc along the jet, the *middle panels* the evolution of the magnetic field, B, in G, and the *bottom panels* show the variation of the maximum and minimum electron Lorentz factors, $\gamma_{\mathrm{min,max}}$. The *solid* and *dashed red lines* correspond to a model where we take both, synchrotron and adiabatic losses into account. In order to demonstrate the influence of radiative losses we computed additionally the evolution of the electron Lorentz factor only for adiabatic losses (*solid* and *dashed lines* in *bottom panels*)

of the magnetic field and the evolution of the electron Lorentz factor $\gamma_{\mathrm{min,max}}$. The red solid and dashed lines in the bottom panels correspond to the variation of the electron Lorentz factor taking synchrotron and adiabatic losses into account and the black solid and dashed lines show the evolution of the electron Lorentz factor assuming only adiabatic losses.

For both jet models, the evolution of the upper electron Lorentz factor, γ_{max}, decreases fast if the synchrotron losses are taken into account. The adiabatic losses are the dominant energy loss mechanism for $r > 3$ pc, which can be deduced from the similar slopes of the solid black and red lines. However, the evolution of the lower electron Lorentz factor, γ_{min}, is hardly affected by synchrotron losses.

The calculations show that in the case of an over-pressured jet, the magnetic field intensity increases at the position of the recollimation shocks (in the plot at $r \sim 20$ pc and $r \sim 270$ pc), and at the same position the electron Lorentz factor increases. This increase of the Lorentz factor corresponds to the local increase of the particle density, i.e., adiabatic compression (see, e.g., Mimica et al. 2009). Farther downstream, the jet expands and the magnetic field and the Lorentz factors decrease again. At the

second recollimation shock, there is again a local increase in both, magnetic field and electron Lorentz factor. This behavior is also visible if we assume only adiabatic losses.

In contrast to the over-pressured jet, the evolution of the magnetic field and the electron Lorentz factor are continuously decreasing in the case of a conical jet (see right panels in Fig. 2.7).

2.2.2 Opacity Variations

Assuming that the position of the observed VLBI core coincides with the ($\tau = 1$)-surface, Marcaide and Shapiro (1983) and Lobanov (1998) used Eq. 2.31 to derive the frequency-dependent position of the core, the so-called core-shift. This core-shift is illustrated in Fig. 2.8 and shows the variation of the distance between the core and an optically thin jet region, whose position is assumed to be frequency independent.

Assuming, a conical jet geometry, i.e., $R \propto r$, a decreasing magnetic field, $B = B_1 r^{-b}$ and a decreasing particle density, $K = K_1 r^{-k}$, where the constants B_1 and K_1 correspond to the magnetic field and electron normalization coefficient at 1 pc, Eq. 2.31 results in:

$$r \propto \nu^{-1/k_r}, \tag{2.46}$$

where $k_r = [2k + 2b\,(3 - 2\alpha_0) - 2]\,/\,(5 - 2\alpha_0)$ and α_0 is the optically thin spectral index.

Measurements of the core-shift can yield estimates of several physical parameters such as the magnetic field and the distance to the central engine (Lobanov 1998; Hirotani 2005; O'Sullivan and Gabuzda 2009; Pushkarev et al. 2012). The core shift measure, $\Omega_{r\nu}$ between two frequencies is defined as:

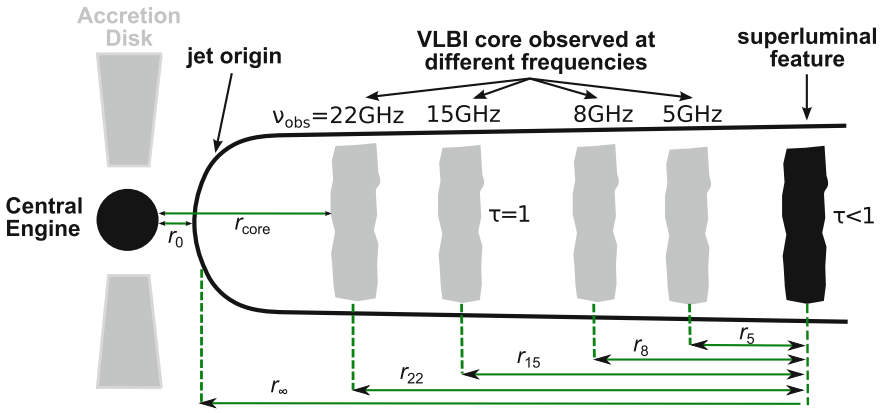

Fig. 2.8 Illustration of the frequency dependence of the core position. Taken from Schinzel (2011)

$$\Omega_{r\nu} = 4.85 \times 10^{-9} \frac{\Delta r_{\nu_1,\nu_2} D_L \nu_1^{1/k_r} \nu_2^{1/k_r}}{(1+z)^2 \left(\nu_2^{1/k_r} - \nu_1^{1/k_r}\right)} \text{ [pc} \times \text{GHz]}, \tag{2.47}$$

with $\Delta r_{\nu_1,\nu_2}$ being the core shift between the frequencies ν_1 and ν_2, in mas, and D_l the luminosity distance, in pc. Following Hirotani (2005) and replacing the jet opening angle φ and the viewing angle ϑ by the more directly measurable apparent speed β_{app}, the magnetic field at 1 pc is given by:

$$B_1 \approx \frac{2\pi m_e^2 c^4}{e^3} \left[\frac{e^2}{m_e c^2} \left(\frac{\Omega_{r\nu}}{r_1 \left(1+\beta_{\text{app}}^2\right)^{1/2}} \right)^{k_r} \right]^{\frac{5-2\alpha_0}{7-2\alpha_0}}$$
$$\times \left[\pi C(\alpha_0) \frac{r_1 m_e c^2}{e^2} \frac{-2\alpha_0}{\gamma_{\text{min}}^{2\alpha_0+1}} K(\gamma, \alpha_0) \left(1+\beta_{\text{app}}\right)^{\frac{-(1+2\alpha_0)}{4}} (1+z)^{\alpha_0 - \frac{3}{2}} \right]^{\frac{-2}{7-2\alpha_0}} \text{[G]}, \tag{2.48}$$

where $C(\alpha_0)$ and $K(\gamma, \alpha_0)$ are defined as:

$$C(\alpha_0) = \frac{3^{1-\alpha_0}}{8} \sqrt{\pi} \hat{\Gamma}\left(\frac{7-2\alpha_0}{4}\right) \hat{\Gamma}\left(\frac{5-6\alpha_0}{12}\right) \hat{\Gamma}\left(\frac{25-6\alpha_0}{12}\right) \hat{\Gamma}\left(\frac{9-2\alpha_0}{4}\right) \tag{2.49}$$

$$K(\gamma, \alpha_0) = \frac{2\alpha_0+1}{2\alpha_0} \frac{\left[(\gamma_{\text{max}}/\gamma_{\text{min}})^{2\alpha} - 1\right]}{\left[(\gamma_{\text{max}}/\gamma_{\text{min}})^{2\alpha+1} - 1\right]} \tag{2.50}$$

The distance to the central engine can be calculated by inserting the value for B_1 (Eq. 2.48) into Eq. 2.31 and solving for r_{core}:

$$r_{\text{core}}(\nu) \approx \Omega_{r\nu} \left(1+\beta_{\text{app}}^2\right)^{1/2} \nu^{-1/k_r} \text{ [pc]} \tag{2.51}$$

The equations above can be simplified if we assume a conical jet, $b = 1$, $k = 2$, equipartition between the magnetic energy density and the kinetic energy density and a spectral index of $\alpha_0 = -0.5$ (which leads to $k_r = 1$, see definition of k_r):

$$B_1 \approx 0.042 \Omega_{r\nu}^{3/4} (1+z)^{1/2} \frac{\left(1+\beta_{\text{app}}^2\right)^{3/8}}{\beta_{\text{app}}^{1/2}} \text{ [G]}, \tag{2.52}$$

$$r_{\text{core}}(\nu) \approx \Omega_{r\nu} \left(1+\beta_{\text{app}}^2\right)^{1/2} \nu^{-1} \text{ [pc]}. \tag{2.53}$$

The particle density N_1 is given by:

$$N_1 = \frac{K(\gamma, \alpha_0)}{8\pi m_e c^2} \gamma_{\min}^{-1} B_1^2. \tag{2.54}$$

If we assume $k_r = 1$, $\alpha_0 = -0.5$ and a ratio of 10^3 between the upper and lower electron Lorentz factors, the equation above can be written as:

$$N_1 = 0.47 \times 10^6 \gamma_{\min}^{-1} B_1^2. \tag{2.55}$$

If we assume that the jet is in equipartition and has a conical geometry, we can calculate the magnetic field using Eqs. 2.48–2.53. In addition, we can derive an estimate for the magnetic field at the core, $B_{\rm core} = B_1 r_{\rm core}^{-1}$ and the relativistic particle density $N_{\rm core} = N_1 r_{\rm core}^{-2}$. These relations are only valid for a conical jet with a dominating toroidal magnetic field. In general the radial evolution of the magnetic field in the jet is given by $B \propto r^{-\epsilon b}$, where ϵ is the jet opening index ($R \propto r^{\epsilon}$) and b parametrizes the evolution of the magnetic field ($B \propto R^{-b}$). For a jet in equipartition the particle density has to decrease as $N \propto R^{-2b}$ or, in terms of distance along the jet $N \propto r^{-2b\epsilon}$ Assuming a conical jet $\epsilon = 1$ and a toroidal magnetic field ($b = 1$) the given relations are obtained.

2.2.3 Shock-In-Jet Model

In the last two sections we only considered the steady-state conditions of a jet. However, to study the flaring process we need to describe the propagation of a shock wave within the unperturbed flow. The shock-in-jet model of Marscher and Gear (1985) describes the evolution of a traveling shock wave in a steady state jet. During the passage of the shock through a steady jet, the relativistic particles are swept up at the shock front and gain energy while crossing it. In this model, the flaring flux density is assumed to be produced by the accelerated particles within a small layer of width x behind the shock front. The width of this layer is assumed to depend on the dominant cooling process and can be approximated by $x \propto t_{\rm cool}$, where $t_{\rm cool}$ is the typical cooling time.

2.2.3.1 Evolutionary Stages

Compton losses: If the photon energy density, $u_{\rm ph}$, is higher than the magnetic energy density, $u_{\rm b} = B^2/(8\pi)$, the inverse Compton scattering is the dominant energy loss mechanism during the first stage of the flare. The width of the layer behind the shock front during this Compton stage, x_1, is computed to be:

$$x_1 \propto B^{1/2} \nu^{-1/2} \delta^{1/2} u_{\rm ph}^{-1}. \tag{2.56}$$

An approximation of the photon energy density, $u_{\rm ph}$, can be obtained by integrating the emission coefficient, ϵ_ν, over the optically thin regime ($\nu_m < \nu < \nu_{\rm max}$)[1], which leads to:

$$u_{\rm ph} \propto K \left(B^{3s+7} R^{s+5} \right)^{1/8}. \tag{2.57}$$

The final expression for the width of the layer behind the shock front during the Compton stage can be written as:

$$x_1 \propto R^{-(s+5)/8} K^{-1} B^{-3(s+1)/8} \delta^{1/2} \nu^{-1/2} \tag{2.58}$$

Synchrotron losses: Synchrotron losses become more important at the point where the photon energy density, $u_{\rm ph}$, is comparable to the magnetic energy density, $u_{\rm b}$. The width of the layer x_2 in the synchrotron stage can be computed by replacing $u_{\rm ph}$ in Eq. 2.56 with $u_{\rm b} = B^2/(8\pi)$ and is given by:

$$x_2 \propto B^{-3/2} \delta^{1/2} \nu^{-1/2}. \tag{2.59}$$

Adiabatic losses: Radiative losses become less important in the last stage of the shock evolution. During this final stage the losses are dominated by the expansion of the source and the width of the layer, x_3, is consistent with the radius of the jet:

$$x_3 \propto R. \tag{2.60}$$

The evolution of the turnover frequencies $\nu_{m,i}$ and turnover flux densities $S_{m,i}$, where i indicates the different energy loss stages (1 = Compton, 2 = synchrotron and 3 = adiabatic loss stage), can be derived by replacing the expressions for R in Eqs. 2.32 and 2.33 with the expression for x_i, assuming that the enhanced emission is produced within this layer of size, x_i, and dropping the coefficients $c_{\kappa/\epsilon}$:

$$\nu_{m,1} \propto (1+z)^{-(s+4)/(s+5)} \, R^{-1/4} B^{1/4} \delta^{(s+3)/(s+5)} \tag{2.61}$$

$$S_{m,1} \propto (1+z)^{(2s+15)/(2s+10)} \, D_L^{-2} R^{11/8} B^{1/8} \delta^{(3s+10)/(s+5)} \tag{2.62}$$

$$\nu_{m,2} \propto (1+z)^{-(s+4)/(s+5)} \left[K^2 B^{s-1} \delta^{s+3} \right]^{1/(s+5)} \tag{2.63}$$

$$S_{m,2} \propto (1+z)^{(2s+15)/(2s+10)} \, D_L^{-2} R^2 \left[K^5 B^{2s-5} \delta^{3s+10} \right]^{1/(s+5)} \tag{2.64}$$

$$\nu_{m,3} \propto (1+z)^{-1} \left[R K B^{(s+2)/2} \delta^{(s+2)/2} \right]^{2/(s+4)} \tag{2.65}$$

$$S_{m,3} \propto (1+z) \, D_L^{-2} \left[R^{2s+13} K^5 B^{2s+3} \delta^{3s+7} \right]^{1/(s+4)} \tag{2.66}$$

Marscher (1990) and Lobanov and Zensus (1999) assumed that the evolution of K, B and δ could be written as a power-law with the jet radius R (notice that in a conical

[1] Marscher and Gear (1985) included only first order Compton scattering.

jet the distance along the jet r is linearly proportional to the jet radius R, $r \propto R$, so the proportionality is preserved):

$$K \propto R^{-k} \quad B \propto R^{-b} \quad \delta \propto R^{-d} \,. \tag{2.67}$$

In this case, a relation between the turnover flux density and the turnover frequency can be found:

$$\nu_{m,i} \propto (1+z)^{p_i} R^{n_i} \tag{2.68}$$

$$S_{m,i} \propto D_L^{-2} (1+z)^{q_i} R^{f_i}, \tag{2.69}$$

which leads to:

$$S_{m,i} \propto D_L^{-2} \, (1+z)^{(q_i n_i - p_i f_i)/n_i} \, \nu_{m,i}^{\epsilon_i}, \tag{2.70}$$

where $\epsilon_i = f_i/n_i$. The exponents f_i, n_i, p_i and q_i include the dependence with the physical quantities B, $N(E)$, K, and D and are defined:

$$n_1 = -(b+1)/4 - d(s+3)/(s+5) \tag{2.71}$$

$$n_2 = -[2k + b(s-1) + d(s+3)]/(s+5) \tag{2.72}$$

$$n_3 = -[2(k-1) + (b+d)(s+2)]/(s+4) \tag{2.73}$$

$$f_1 = (11-b)/8 - d(3s+10)/(s+5) \tag{2.74}$$

$$f_2 = 2 - [5k + b(2s-5) + d(3s+10)]/(s+5) \tag{2.75}$$

$$f_3 = [2s + 13 - 5k - b(2s+3) - d(3s+7)]/(s+4) \tag{2.76}$$

$$p_1 = -(s+4)/(s+5) \tag{2.77}$$

$$p_2 = -(s+4)/(s+5) \tag{2.78}$$

$$p_3 = -1 \tag{2.79}$$

$$q_1 = (2s+15)/(2s+10) \tag{2.80}$$

$$q_2 = (2s+15)/(2s+10) \tag{2.81}$$

$$q_3 = 1. \tag{2.82}$$

The typical evolution of a flare in the turnover frequency—turnover flux density ($\nu_m - S_m$) plane can be obtained by inspecting the R-dependence of the turnover frequency, ν_m, and the turnover flux density, S_m. For a typical set of parameters: $b = 1$, $s = 2.5$, $k = 3$ (assuming an adiabatic flow, $k = 2(s+2)/3$, and $d = 0.02$ corresponding to a nearly constant velocity for a fixed viewing angle, these parameters lead to a set of exponents n_i and f_i, which are summarized in Table 2.2.

During the first stage, in which Compton losses are dominant, the turnover frequency decreases with radius while the turnover flux density increases. In the second stage, in which synchrotron losses are the dominating energy loss mechanism, the turnover frequency continues to decrease while the turnover flux density remains constant. Both the turnover frequency and turnover flux density decrease in the final,

Table 2.2 Values of the indices used in the generalized spectrum expression of Eq. 2.70, n_i and f_i for $b = 1$, $s = 2.5$, $k = 3$, and $d = 0.02$

Stage	n_i	f_i	ϵ
Compton	−0.52	1.2	−2.3
Synchrotron	−1.01	−0.06	0.06
Adiabatic	−1.32	−0.82	0.62

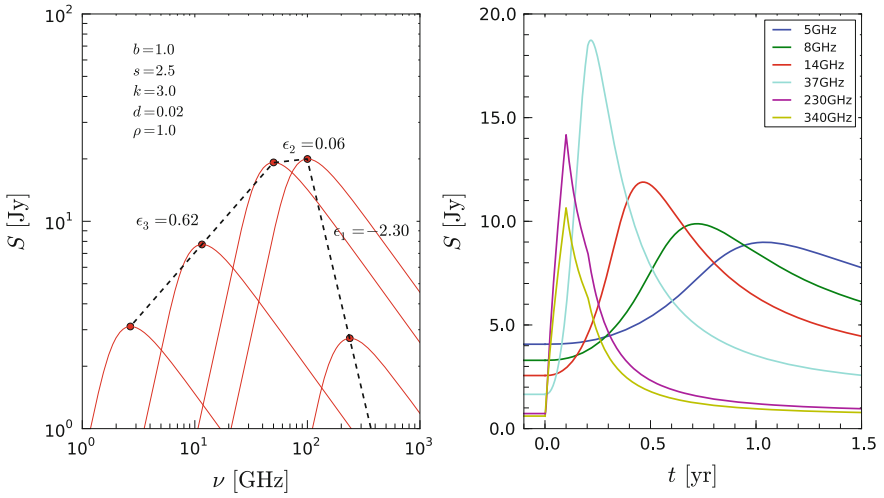

Fig. 2.9 Spectral evolution of a flare computed from the shock-in-jet model with the parameters presented in Table 2.2. *Left* The *dashed black line* corresponds to the evolution of the turnover frequency and turnover flux density during the flare. The slope of the different stages is indicated in the plot and the *red lines* show some example spectra during the evolution. *Right* Single *dish light* curves calculated from the spectral evolution for different frequencies. The zero time is set to the onset of the flare and the flux densities for $t < 0$ correspond to the flux density of the quiescent spectrum

adiabatic stage. Figure 2.9 shows the evolution of a flare using the shock-in-jet model with the parameters presented in Table 2.2.

2.2.3.2 Generalization of the shock-In-Jet Model

Türler et al. (2000) expanded the shock-in-jet model to non-conical jets, e.g., the distance along the jet, r, is no longer a linearly proportional to the jet radius, R. This modification is expressed by $R \propto r^{\rho}$ with $(-1 < \rho < 1)$, which represents a collimating ($\rho < 0$) or expanding ($\rho > 0$) jet. An important implication of allowing non-conical jets ($\rho \neq 1$) in the shock-in-jet model is the r-dependence of the evolution of the spectral parameters (b, k and d). Therefore the evolution of B, K and δ

along the jet is given by:

$$K \propto r^{-\rho k}, \quad B \propto r^{-\rho b}, \quad \delta \propto r^{-\rho d}. \tag{2.83}$$

Besides the modification of the jet geometry, Türler et al. (2000) parametrized the temporal evolution of the turnover frequency, ν_m, and the turnover flux density, S_m, using the equations of superluminal motion[2]

$$t = \frac{r}{\mathrm{v_{obs}}}, \tag{2.84}$$

where $\mathrm{v_{obs}} = (\beta_{\mathrm{app}} c)/((1+z)\sin\vartheta)$. Using the definition of the apparent speed, $\beta_{\mathrm{app}} = (\beta \sin\vartheta)/(1-\beta\cos\vartheta)$, the bulk Lorentz factor, Γ, and the Doppler factor, δ, the equation above results in

$$t = \frac{1+z}{\beta c \delta \Gamma} L. \tag{2.85}$$

Assuming that $\beta \sim 1$ and $\vartheta \sim 1/\Gamma \ll 1$, it can be shown that $\Gamma \propto \delta$ (Taylor expanding $\cos 1/\Gamma$ in the definition of δ). Including the non-conical jet geometry ($R \propto L^r$) the equation above can be written as

$$t \propto (1+z)\delta^{-2} R^{1/\rho} \propto (1+z) R^{\zeta}, \tag{2.86}$$

where $\zeta = (2d\rho + 1)/\rho$. By replacing R in Eqs. 2.68 and 2.69 by Eq. 2.86, the temporal evolution of the turnover frequency and turnover flux density is:

$$\nu_m \propto (1+z)^{(p_i\zeta - n_i)/\zeta} \cdot t^{n_i/\zeta} \tag{2.87}$$

$$S_m \propto D_L^{-2} (1+z)^{(q_i\zeta - f_i)/\zeta} \cdot t^{f_i/\zeta}. \tag{2.88}$$

The equations above can be further simplified by replacing $D_L \propto (1+z)$, which leads to:

$$S_m \propto (1+z)^{[(q_i-2)\zeta - f_i]/\zeta} \cdot t^{f_i/\zeta}. \tag{2.89}$$

2.2.3.3 Modification of the Compton Stage

The determination of the distance that the relativistic particles travel behind the shock front before losing most of their energy is a crucial parameter in shock-in-jet models. Björnsson and Aslaksen (2000) presented a different derivation of this distance than previous works, including the possibility of multiple Compton scattering (in the Thompson regime) during the first rising phase of the flare. In the case of first order Compton scattering, the slope of the Compton stage would be less steep as predicted by Marscher and Gear (1985). Therefore, the existence of a synchrotron stage is no

[2] The time used here was that in the observers frame.

longer needed. The evolution of the turnover-flux density and the turnover frequency with distance (or time) is given, within the model of Björnsson and Aslaksen (2000), by:

$$\nu_m \propto R^{-[4(s+2)+3b(s+4)]/[3(s+12)]} \tag{2.90}$$

$$S_m \propto R^{-[4(s-13)+6b(s+2)]/[3(s+12)]}, \tag{2.91}$$

assuming no changes in the Doppler factor and constant velocity of the shocked particles. Using the same set of parameters as in Table 2.2 gives $n_1 = -0.9$ and $f_1 = 0.3$, resulting in a less steep slope $\epsilon_1 = f_1/n_1 = -0.3$ in the $\nu_m - S_m$-plane which is flatter than in Marscher and Gear (1985) case.

2.2.3.4 Evolution of the Brightness Temperature T_b

The equations presented so far require the knowledge of the evolution of the turnover frequency and turnover flux density to model the flare and to obtain the evolution of the source intrinsic parameters. Therefore, multi-frequency single dish or multi-frequency VLBI observations are needed. However, for most of the sources, simultaneous multi-frequency VLBI observations are not available. In order to apply the model and obtain the relevant information to single frequency VLBI observations one can rewrite the equations presented in this chapter in terms of the brightness temperature, which is defined as:

$$T_\mathrm{b} = 1.22 \times 10^{12} S_\nu R^{-2} \nu^{-2} (1+z) \ \mathrm{[K]} \tag{2.92}$$

where S_ν is the flux density in Jy, R is the width of the jet in mas and ν is the observing frequency in GHz. Some physical conditions, such as the evolution of the magnetic field in the source can be derived from the brightness temperature (e.g., Kadler et al. 2004; Schinzel et al. 2012). The optically thin flux density is given by Eq. 2.32 and the size of the emission region depends on the main depends on the main energy loss mechanism, namely Compton (1), synchrotron (2) and adiabatic losses (3) see Eqs. 2.58–2.60. Inserting the equations above into Eq. 2.32 leads to:

$$S_{\nu,1} \propto R^{-(s-11)/8} \delta^{(s+4)/2} B^{(s+1)/8} \nu^{-s/2} \tag{2.93}$$

$$S_{\nu,2} \propto R^2 \delta^{(s+4)/2} K B^{(s-2)/2} \nu^{-s/2} \tag{2.94}$$

$$S_{\nu,3} \propto R^3 \delta^{(s+3)/2} K B^{(s+1)/2} \nu^{-(s-1)/2}. \tag{2.95}$$

If we assume that the magnetic field, B, the normalization coefficient of the relativistic electron distribution, K, and the Doppler factor, δ, follow a power law with the jet radius:

$$B \propto R^{-b} \quad K \propto R^{-k} \quad \delta \propto R^{-d}, \tag{2.96}$$

Equations 2.93–2.95 can be written in terms of the jet radius:

$$S_{\nu,i} \propto R^{p_i} \nu^{q_i}, \tag{2.97}$$

where the exponent p_i includes the dependencies on B, K and δ and the exponent q_i includes the dependence on the frequency. For the different stages, they are defined as:

$$p_1 = -(s-11)/8 - b(s+1)/8 - d(s+4)/2 \tag{2.98}$$
$$p_2 = 2 - b(s-2)/2 - d(s+4)/2 - k \tag{2.99}$$
$$p_3 = 3 - b(s+1)/2 - d(s+3)/2 - k \tag{2.100}$$
$$q_1 = -s/2 \tag{2.101}$$
$$q_2 = -s/2 \tag{2.102}$$
$$q_3 = -(s-1)/2. \tag{2.103}$$

In order to generalize these equations to non-conical jets, the distance along the jet, r, is no longer directly proportional to the jet radius R. This modification is expressed by $R \propto r^{\rho}$ where $-1 < \rho < 1$. Finally, we can write the evolution of the brightness temperature as:

$$T_{\rm b} \propto r^{\epsilon_i} \nu^{q_i - 2}, \tag{2.104}$$

where the exponent ϵ_i is given, for the different stages, by:

$$\epsilon_1 = \rho\,[-(s+5)/8 - b(s+1)/8 - d(s+4)/2] \tag{2.105}$$
$$\epsilon_2 = \rho\,[-b(s-2)/2 - d(s+4)/2 - k] \tag{2.106}$$
$$\epsilon_3 = \rho\,[1 - b(s+1)/2 - d(s+3)/2 - k]\,. \tag{2.107}$$

The equations above can be further simplified (i. e., dropping the k dependence in the equations above) if we assume adiabatic expansion $k = k_{\rm ad} = 2(s+2)/3$ and equipartition between the magnetic energy density, $\mathcal{E}_{\rm mag} \propto B^2$, and the kinetic energy density, $\mathcal{E}_{\rm kin} \propto K$, which leads to $b = b_{\rm eq} = (s+2)/3$:

$$\epsilon_1^{\rm ad,eq} = \rho\left[-(s^2+5s+12)/16 - d(s+4)/2\right] \tag{2.108}$$
$$\epsilon_2^{\rm ad,eq} = \rho\left[-(s^2+4s+8)/6 - d(s+4)/2\right] \tag{2.109}$$
$$\epsilon_3^{\rm ad,eq} = \rho\left[-(s^2+7s+4)/6 - d(s+3)/2\right]. \tag{2.110}$$

These relations can be used to derive the parameter range for exponents ρ, s, k, b and d using the observed evolution of the brightness temperature at a given frequency.

2.3 Superluminal Motion and the Relativistic Beam of Radiation

Some of the observed and traced features at the parsec scale of jets show exhibit an speed which is larger than the speed of light. This apparent superluminal motion can be explained by intrinsic velocities close to the speed of light and a projection of the 3D geometry into the sky plane by a small angle to the line of sight (Rees 1967).

Assuming a source of relativistic motion located in the sky which has a viewing angle, ϑ, to an observers. Lets assume a blob of plasma moves at a velocity $\beta = v/c$ and emits a photon at the location A at $t = t_0$ and at the location B at $t = t_1$ (see Fig. 2.10). The distance the blob has travelled in the source frame AB is given by $\beta c \Delta t_e$, where $\Delta t_e = t_1 - t_0$. Within the time interval Δt_e the blob has travelled the distance AC $= \beta c \Delta t_e \cos\vartheta$ in the observers frame and the photon emitted in A have travelled the distance AD $= c\Delta t_e$. The distance between the two photons emitted in A and B is equal to the distance CD $= c\Delta t_e(1 - \beta\cos\vartheta)$ and their time difference in the observers frame is $\Delta t_o = \mathrm{CD}/c = \Delta t_e(1 - \beta\cos\vartheta)$. In the observes frame the distance between the two locations of the blob is CB $= \beta c \Delta t_e \sin\vartheta$ from which the apparent velocity β_{app} follows:

$$\beta_{\mathrm{app}} = \frac{\beta \sin\vartheta}{1 - \beta\cos\vartheta} \tag{2.111}$$

The maximum apparent speed is obtained if the features are travelling at the critical angle, the angle that maximizes the speed of the feature. The critical viewing angle, $\vartheta_{\mathrm{crit}}$ can be derived by calculating the derivative of the apparent speed with respect to ϑ for any given β. This leads to the result that the maximum apparent speed is obtained if $\cos\vartheta_{\mathrm{crit}} = \beta = \left[\beta_{\mathrm{app}}^2/(1 + \beta_{\mathrm{app}}^2)\right]^{1/2}$. For jets seen at this critical angle, the Doppler factor is:

$$\delta_{\mathrm{crit}} = \sqrt{1 + \beta_{\mathrm{app}}^2}. \tag{2.112}$$

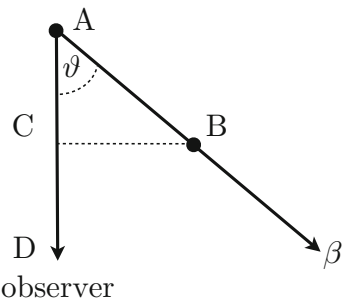

Fig. 2.10 Illustration of for the de-projection of superluminal motion

From Eq. 2.112 follows that the existence of relativistic motions (apparent speeds) give rise to large Doppler factors. Relativistic aberration leads to a forward boosting of the emission of an electron into a cone with half-opening angle similar to the inverse of the bulk Lorentz factor. Therefore, the flux density increases by a factor δ^2. Additionally, the frequency is Doppler shifted which results into a final boosting of the flux density (see, e.g., Marscher 2006):

$$S_\nu \propto \delta^{2-\alpha} \nu^{+\alpha} \quad \text{steady state} \tag{2.113}$$

$$S_\nu \propto \delta^{3-\alpha} \nu^{+\alpha} \quad \text{moving feature .} \tag{2.114}$$

References

Begelman, M. C., Blandford, R. D., & Rees, M. J. 1984, Reviews of Modern Physics, 56, 255.
Björnsson, C.-I. & Aslaksen, T. 2000, Astrophys. J., 533, 787.
Daly, R. A. & Marscher, A. P. 1988, Astrophys. J., 334, 539.
Falle, S. A. E. G. 1991, MNRAS, 250, 581.
Fromm, C. M., Perucho, M., Ros, E., et al. 2011, A&A, 531, A95.
Fromm, C. M., Ros, E., Perucho, M., et al. 2013a, A&A, 551, A32.
Fromm, C. M., Ros, E., Perucho, M., et al. 2013b, A&A, 557, A105.
Georganopoulos, M. & Marscher, A. P. 1998, Astrophys. J., 506, 621.
Hardee, P. E., Bridle, A. H., & Zensus, J. A. 1996, Astronomical Society of the Pacific Conference Series, 100.
Hardee, P. E. 2000, Astrophys. J., 533, 176.
Hardee, P. E. & Eilek, J. A. 2011, Astrophys. J., 735, 61.
Hirotani, K. 2005, Astrophys. J., 619, 73.
Jorstad, S. G., Marscher, A. P., Lister, M. L., et al. 2005b, Astron. J., 130, 1418.
Kadler, M., Ros, E., Lobanov, A. P., Falcke, H., & Zensus, J. A. 2004, A&A, 426, 481.
Komissarov, S. S. & Falle, S. A. E. G. 1997, MNRAS, 288, 833.
Konigl, A. 1981, Astrophys. J., 243, 700.
Lind, K. R. & Blandford, R. D. 1985, Astrophys. J., 295, 358.
Lobanov, A. P. 1998, A&A Supplement, 132, 261.
Lobanov, A. P. & Zensus, J. A. 1999, Astrophys. J., 521, 509.
Marcaide, J. M. & Shapiro, I. I. 1983, Astron. J., 88, 1133.
Marscher, A. P. 1987, IN: Superluminal radio sources; Proceedings of the Workshop, 280.
Marscher, A. P. 1990, Parsec-scale radio jets, 236.
Marscher, A. P. 2006, Relativistic Jets: The Common Physics of AGN, 856, 1.
Marscher, A. P. & Gear, W. K. 1985, Astrophys. J., 298, 114.
Martí, J. M. A., Mueller, E., Font, J. A., Ibáñez, J. M. A., & Marquina, A. 1997, Astrophys. J., 479, 151.
Martí, J. M. & Müller, E. 1999, Living Reviews in Relativity, 2, 3.
Mimica, P., Aloy, M.-A., Agudo, I., et al. 2009, Astrophys. J., 696, 1142.
Nalewajko, K. & Sikora, M. 2009, MNRAS, 392, 1205.
O'Sullivan, S. P. & Gabuzda, D. C. 2009, MNRAS, 400, 26.
Pacholczyk, A. G. 1970, Radio astrophysics. Nonthermal processes in galactic and extragalactic sources, W. H. Freeman & Company.
Perucho, M. 2005, PhD thesis, Universitat de València, Spain.
Perucho, M. & Martí, J. M. 2007, MNRAS, 382, 526.
Perucho, M. 2012, International Journal of Modern Physics: Conference Series, 08, 241.

Pushkarev, A. B., Hovatta, T., Kovalev, Y. Y., et al. 2012, eprint arXiv, 1207, 5457.
Pushkarev, A. B., Kovalev, Y. Y., Lister, M. L., & Savolainen, T. 2009, A&A, 507, L33.
Rees, M. J. 1967, MNRAS, 135, 345.
Schinzel, F. K. 2011, PhD thesis, University of Cologne, Germany.
Schinzel, F. K., Lobanov, A. P., Taylor, G. B., et al. 2012, A&A, 537, 70.
Türler, M., Courvoisier, T. J.-L., & Paltani, S. 1999, A&A, 349, 45.
Türler, M., Courvoisier, T. J.-L., & Paltani, S. 2000, A&A, 361, 850.

http://www.springer.com/978-3-319-10767-7

Spectral Evolution in Blazars
The Case of CTA 102
Fromm, C.
2015, XVI, 210 p. 127 illus., 112 illus. in color.,
Hardcover
ISBN: 978-3-319-10767-7